Development of An Optimal Low-Noise Voice-Coil Actuator for Precision Motion Control Applications

Suorena Saeedi , Ali Sadighi* , Masoud Shariat Panahi

School of Mechanical Engineering, College of Engineering, University of Tehran, Tehran, Iran

ABSTRACT: Voice-Coil Actuators (VCAs) serve as indispensable components in precision motion applications, valued for their linear force performance, smooth operation, and compact size. The optimal design of VCAs not only contributes to cost reduction in manufacturing and assembly but also results in a more compact size and increased bandwidth, enhancing VCA's overall performance. On the other hand, developing a model that captures the nonlinear features of actuator dynamics is essential for advancing high-performance controllers. In addition, such a model can be very useful in simulating the performance of controllers before implementation, as well as studying the behavior of different parts of the actuator during its operation. This paper introduces a novel approach to VCA design through a multi-objective optimization problem solved using the Non-Dominated Sorting Genetic Algorithm-II (NSGA-II). Once the optimal design is determined, it undergoes validation via finite-element analysis. After validating the optimal design, the actuator is fabricated and assembled through a detailed electromechanical design. To mitigate potential noise issues arising from switching circuits, the study proposes a high-bandwidth analog servo amplifier. This amplifier is designed to effectively mitigate noise problems, ensuring the seamless operation of the VCA in practical applications. Before modeling, the characterization process is undertaken through a combination of simulation and experimental tests. Finally, the effectiveness of the multi-physics-based modeling approach, enhanced by experimentally-driven characteristics, is evaluated against empirical results.

1- Introduction

The term Voice-Coil Actuator (VCA) a non-commutated dc linear actuator, comes from one of its historically first applications: vibrating the paper cone of a loudspeaker. Today they are used for a wide range of precision motion applications. VCAs are widely utilized owing to their advantages over conventional linear actuators. These actuators are distinguished by their straightforward design, rapid response, high acceleration, and efficient conversion of electrical to mechanical energy. Their versatility allows for a broad spectrum of applications [1-11]. Also, these actuators are frequently employed in precision motion applications since they are free from mechanical hysteresis, force ripple, and backlash, due to their non-contact and continuous performance [12-14]. These benefits have led to the usage of voice coil actuators in a variety of applications, including fuel injection systems [15], computer disk drives [16], audio loudspeakers [9], air bearings [12], needle-free jet injection [17], etc. The space occupied by the actuator is critical in many of these applications, therefore optimizing the actuator's dimensions can be vital.

There are different shapes of VCAs, but cylindrical VCA is the most prevalent type and it has numerous applications. So, the optimal design of Cylindrical VCAs (CVCAs) has drawn plenty of attention from diverse research fields. To minimize the overall mass of CVCA, a combination of the improved sequential optimization method (SOM) and the dimension reduction optimization method (DROM) is proposed in [18]. The sequential quadratic programming (SQP) algorithm is also used in [17] to optimize the CVCA mass of a needle-free jet injection system. The geometric dimensions of a CVCA are minimized in [19] using a single-objective optimization method in which the objective function is defined as a combination of geometric dimensions, and then the Space Mapping (SM) method is used to minimize the objective function while taking into account the constraints. By solving a multi-objective optimization problem to maximize acceleration and reduce heat loss, the optimal design for a CVCA is achieved in [12]. In [20], an optimal design was established to minimize the response time of a CVCA, which is required in fast-switching valves. And in [15], main structural parameters of a CVCA used in a fuel injection system was optimized by the magnetic equivalent circuit (MEC) method to maximize the flow rate of the injector.

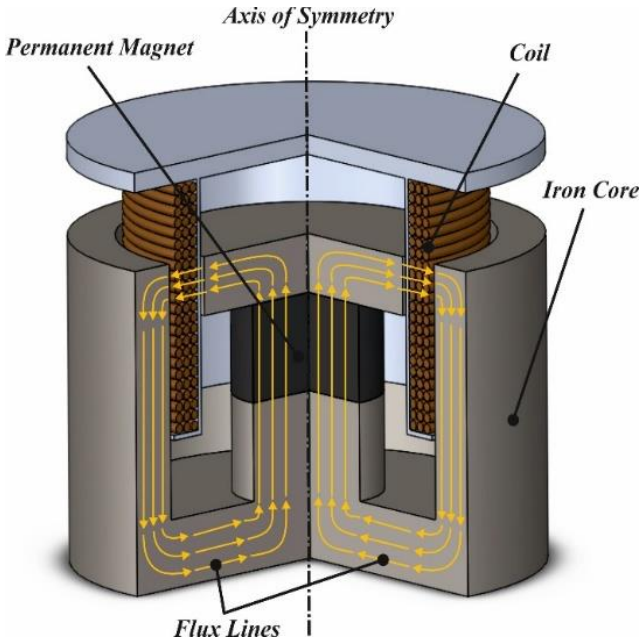*Corresponding author's email: asadighi@ut.ac.ir

Fig. 1. CVCA schematic.

Fig. 2. Design parameters of CVCA, magnetic circuit.

The modeling of CVCAs is also quite beneficial. An actuator model may be used to try out different control architectures, reducing the amount of experimental trial and error and operating expenses.

Most of the CVCA models [21-23] fail to consider system nonlinearities such as variable force constant, temperature dependency, control effort saturation, and so on.

In this paper, the development of an optimally-designed CVCA and its comprehensive modeling is carried out. First, CVCA design is formulated as a multi-objective optimization problem and NSGA-II is used to solve this problem. after validating the optimal design via finite-element analysis and fabricating through detailed electromechanical design, a multi-physics-based mode considering CVSAs non-linear behavior is introduced. Finally, the performance of this model is evaluated and it is compared with experimental results. Also, in this paper, a high-bandwidth analog servo amplifier is proposed to effectively mitigate noise problems, and ensure the seamless operation of the VCA in practice.

In section 2, CVCA design is formulated as a multi-objective optimization problem to minimize the overall actuator dimensions. Finite-element analysis is performed to validate the optimal design. The electromechanical design of the actuator is the subject of Section 3. A high-bandwidth servo amplifier is used to regulate current quickly and smoothly. The characterization of the CVCA is discussed in Section 4, where the actuator force constant, and the fundamental mechanical characteristics such as mass, stiffness, and damping, are empirically identified. In Section 5, a thorough model of the actuator is established. The system dynamics are determined by the interaction of mechanical, electrical, and thermal subsystems in this model. The validity of the developed model is demonstrated by the experimental results.
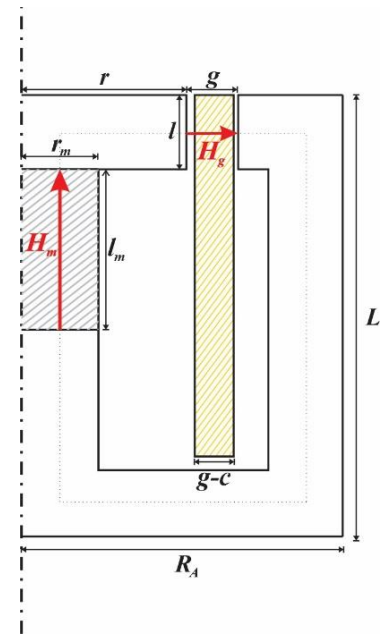
2- Optimal magnetic design

2- 1- Magnetic circuit

CVCA includes a cylindrical iron core with a permanent magnet in the center and a cylindrical coil located inside the air gap carrying current perpendicular to the flux lines. Fig. 1 shows various parts of a CVCA.

According to the Lorentz force law:

$$F = i_w l_w B_g \tag{1}$$

Where F represents the Lorentz force in the direction of the axis of symmetry, i_w represents the current of the coil, l_w represents the length of the coil wire through which the flux lines pass, and B_g is the magnitude of the magnetic flux density in the air gap.

In our analysis, we make the following assumptions:

The relative permeability of the iron core is infinite and hence the magnetic field is zero throughout the iron core.

The magnetic flux is contained in the actuator body (zero flux leakage) and there is no flux fringing in the air gap.

Given these assumptions and the axisymmetric nature of the problem, the main parameters of interest are shown in Fig. 2 where the magnetic fields only exist in the magnet and the air gap. The geometric parameters shown in lowercase, are determined through optimization as discussed later in this section. Overall length, L_A, and outer radius, R_A, are then obtained based on these geometries, stroke of the actuator, and magnetic saturation considerations.

Also, according to Fig. 2, the length of the coil wire through which the flux lines pass can be estimated as follows:

$$l_w = 2\pi N_w \left(r + g / 2\right) \tag{2}$$

Where N_w represents the number of coil wires through which the flux lines pass, r represents the internal radius of the iron core, and g is the length of the air gap. Also, by considering the concept of the current density (J), the current of the coil can be calculated as follows:

$$i_w = l(g-c)J/N_w \tag{3}$$

Where c is clearance between coil and actuator stator, so according to equations 1, 2, and 3, the equation of Lorentz force can be written as follows:

$$F = 2\pi(r+g/2)l(g-c)JB_g \tag{4}$$

Also according to the Ampere's law:

$$\oint_C H.dl = 0 \rightarrow H_m = -\frac{g}{l_m\mu_0}B_g \tag{5}$$

Where H_m represents the magnetic field of the permanent magnet, l_m represents length of the permanent magnet, and μ_0 is the air permeability and its value is $4\pi\times10^{-7}$ H/M. Also according to the Gauss's law:

$$\oint B.da = 0 \rightarrow B_m = \frac{2rl}{r_m^2}B_g \tag{6}$$

Where B_m represents the magnitude of the magnetic flux density in the permanent magnet, and r_m is the radius of the permanent magnet.

The following equation can also be used to estimate the equivalent resistance of the coil:

$$R = \rho L_w/A \tag{7}$$

Where R represents the equivalent resistance of the coil, ρ represents the resistivity, and assuming that the coil wire is made of copper, its value is equal to $1.68\times10^{-8}\,\Omega.\text{m}$, L_w represents the whole length of the coil wire, and A is the cross-sectional area of the wire, which can be estimated as follows:

$$A = (g-c)(l+s)/N \tag{8}$$

Where s represents actuator stroke length, and N is the number of the coil wire, L_w can also be estimated as follows:

$$L_w = 2\pi N(r+g/2) \tag{9}$$

So, according to (7), (8), and (9) equivalent resistance of the coil can be written as follows:

$$R = 2\pi\rho N^2 \frac{(r+g/2)}{(g-c)(l+s)} \tag{10}$$

And the coil current calculated in (3) can be written in another way:

$$i_w = (l+s)(g-c)J/N \tag{11}$$

Also, according to (10), and (11) the supply voltage of the coil can be calculated as follows:

$$V = i_wR = 2\pi\rho NJ(r+g/2) \tag{12}$$

Finally, according to (11), and (12) the electrical power of the actuator can be calculated as follows:

$$P = i_wV = 2\pi\rho J^2(r+g/2)(g-d)(l+s) \tag{13}$$

2- 2- Optimization

In the previous section, the CVCA governing electromagnetic equations were obtained. In this section, we try to define a multi-objective optimization problem through these equations to achieve the optimal design of the actuator.

The first objective of this optimization is to minimize the internal radius of the iron core (r) because reducing r not only reduces the mass and space occupied by the actuator but also reduces the internal radius of the coil, which in turn reduces the mass of the rotor. According to (4) and (5), the internal radius of the iron core can be calculated according to design parameters:

$$r = \frac{B_gF + \pi H_m l_m \mu_0 (-H_m l_m \mu_0 - c)lJ}{2\pi(-H_m l_m \mu_0 - c)lJB_g} \tag{14}$$

The second objective is to minimize the air gap (g), which directly reduces coil mass and increases actuator bandwidth. Based on (5), the air gap can be written based on design parameters:

$$g = -\frac{H_m l_m \mu_0}{B_g} \tag{15}$$

The third and final objective of optimization is to minimize the radius of the permanent magnet (r_m) because it reduces the cost of manufacturing and assembling the CVCA. According to (4), (5), and (6) radius of the permanent magnet
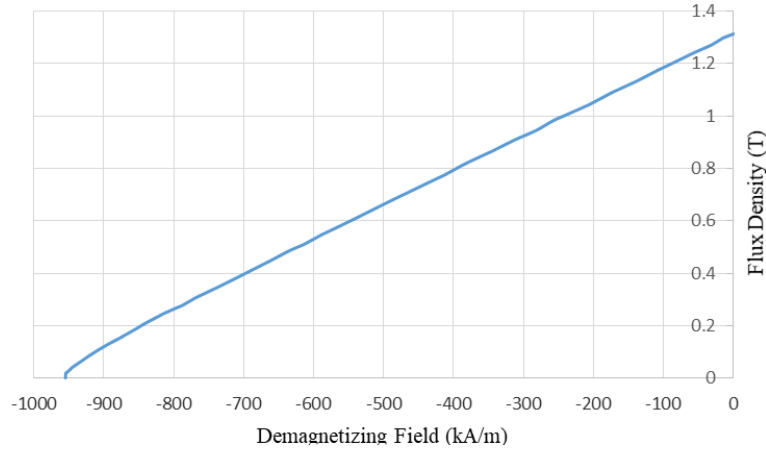
Fig. 3. B-H curve of grade 42 neodymium-iron-boron magnet at 20

can be calculated according to design parameters:

$$r_m = \sqrt{\frac{B_g F + \pi H_m l_m \mu_0 l J \left(-H_m l_m \mu_0 - c \right)}{\pi B_m J \left(-H_m l_m \mu_0 - c \right)}} \qquad (16)$$

It is assumed that Grade 42 neodymium-iron-boron (NdFeB) Magnet is used in the design of this actuator. There is also a tendency for the magnet to work in a zone where the magnet energy is maximum.

The energy of the magnet (E_m) is the product of the magnetic flux density and the magnetic field of the magnet, and assuming that the working temperature of the magnet is 20 ℃ , according to Fig. 3, the working point at which the magnet has the most energy is as follows:

$$\frac{dE_m}{dH_m} = 0 \rightarrow \begin{cases} H_m = -477.5 kA/m \\ B_m = 0.65 T \end{cases}$$

Also, according to the application of the CVCA, its force (F) is considered equal to 15N and its stroke (s) is equal to 65mm. Due to the manufacturing constraints, the value of the clearance (c) is considered equal to 2mm.

Another constraint on this problem is that the electrical power of the actuator should not exceed 40w:

$$P \le P_{max} = 40w$$

Besides, according to the actuator's geometry, we know that the radius of the permanent magnet (r_m) should not be less than zero and not greater than the internal radius of the iron core (r).

$$0 < r_m \le r$$

And as a final constraint, we know that the thickness of the coil (g-c) must be greater than zero.

Therefore, the optimization model is defined as follows:

$$\text{Min}: \begin{cases} r: internal\ radius\ of\ the\ iron\ core \\ g: air\ gap \\ r_m: radius\ of\ the\ permanent\ magnet \end{cases}$$

$$s.t \begin{cases} g_1: H_m = -477.5\ kA/m \\ g_2: B_m = 0.65\ T \\ g_3: F = 15\ N \\ g_4: s = 65\ mm \\ g_5: c = 2\ mm \\ g_6: P \le P_{max} = 40\ W \\ g_7: 0 < r_m \le r \\ g_8: g - c > 0 \end{cases}$$

Table 1 shows the design parameters and the acceptable range of their changes. In the next step, this multi-objective optimization problem is solved using the NSGA-II, and to do so, the optimization toolbox of MATLAB 2018b is used.

In the optimization toolbox, the gamultiobj solver is considered to use the NSGA-II to solve the problem and after defining the mentioned multi-objective optimization problem, the optimization parameters are set as shown in Table 2. Other settings are set to the default value and then the algorithm is run.

Finally, the algorithm converges after 1371 generations and the Pareto optimal front can be seen in Fig. 4. Since it contains non-dominated points, each point can represent an optimal design. Finally, considering the manufacturing constraints and manufacturing and assembly costs, a point of Pareto optimal front has been selected as the final optimal design.

So, the optimal design acquired from the NSGA-II, which includes the objective functions and variables of the selected point from the Pareto optimal front, can be seen in Table 3.

308

Table 1. The design parameters and ranges.

Par	Definition	Unit	Min	Max
B_g	Magnitude of the magnetic flux density in the air gap	T	0	2
J	Current density in the coil	A / mm^2	0	6.5
l_m	Length of the permanent magnet	mm	0	900
l	The length required to cross the magnetic flux	mm	0	90

Table 2. Optimization parameters.

Parameter	Value
Initial population	1000
Crossover fraction	0.75
Function tolerance	10^{-5}
Constraint tolerance	10^{-6}
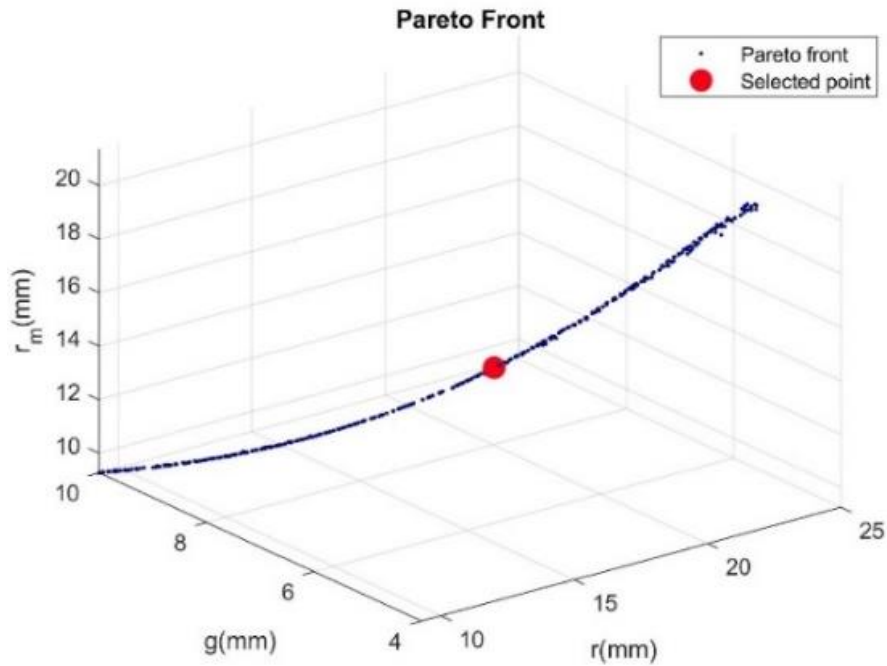
Fig. 4. Pareto optimal front and the point selected as the optimal design.

Table 3. Optimal design parameter of CVCA.

Par	Unit	Value
r	mm	15
g	mm	5
r_m	mm	15
J	A / mm^2	6
l_m	mm	60
l	mm	6
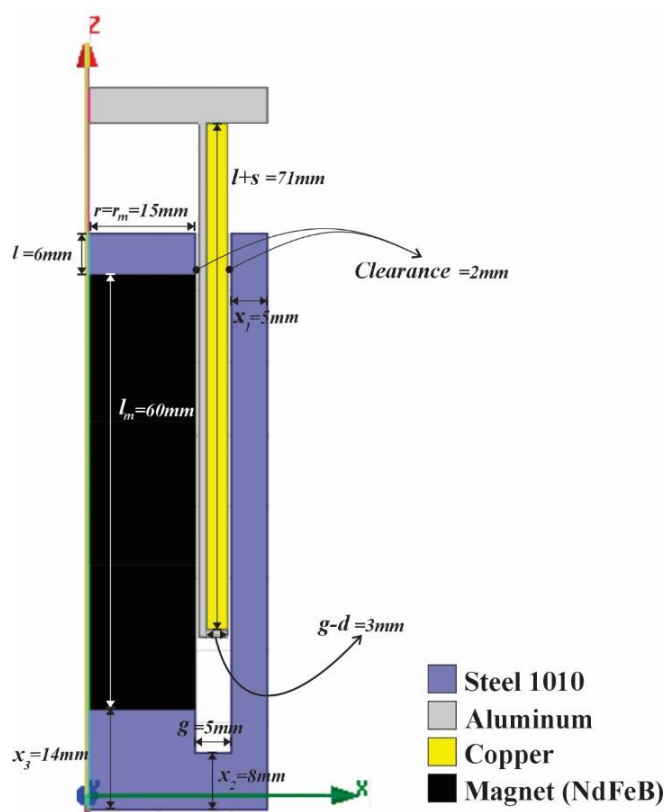
Fig. 5. Optimal design of the CVCA.

2- 3- Finite element analysis

In this section, according to the optimal design parameters obtained in the previous section, the CVCA is simulated and its performance is investigated. ANSYS Maxwell 16 is used to simulate the actuator's performance. In this simulation, the iron core is made of steel 1010, the coil is made of copper, and the permanent magnet is made of Grade 42 NdFeB. The coil is also mounted on an aluminum rotor so as not to affect the actuator's magnetic circuit.

Parameters x_1, x_2, and x_3 depicted in Fig. 5, which determine the thickness of the stator have been selected based on experience so that electromagnetic saturation does not occur in the iron core. These parameters do not play a significant role in the actuator's performance and their size should be chosen so large that the saturation in the iron core does not occur. Therefore, their size depends to some extent on the iron core material. Fig. 5 indicates the optimal design of the operator, which shows all the dimensions and the
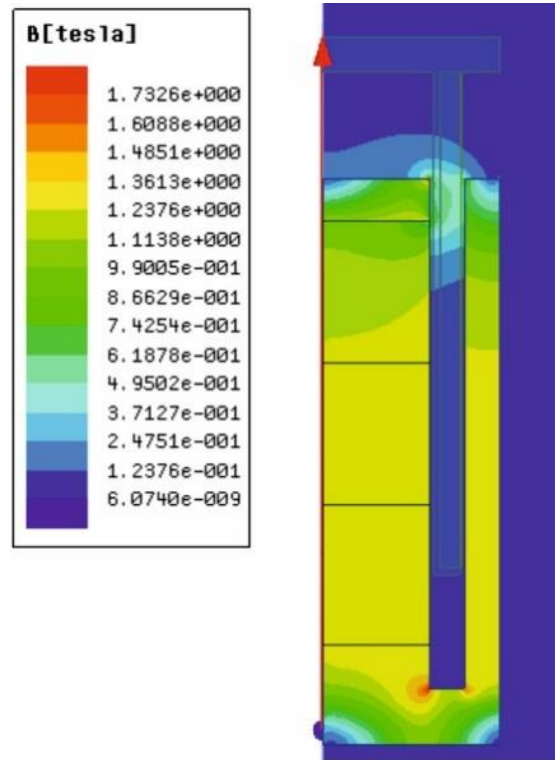
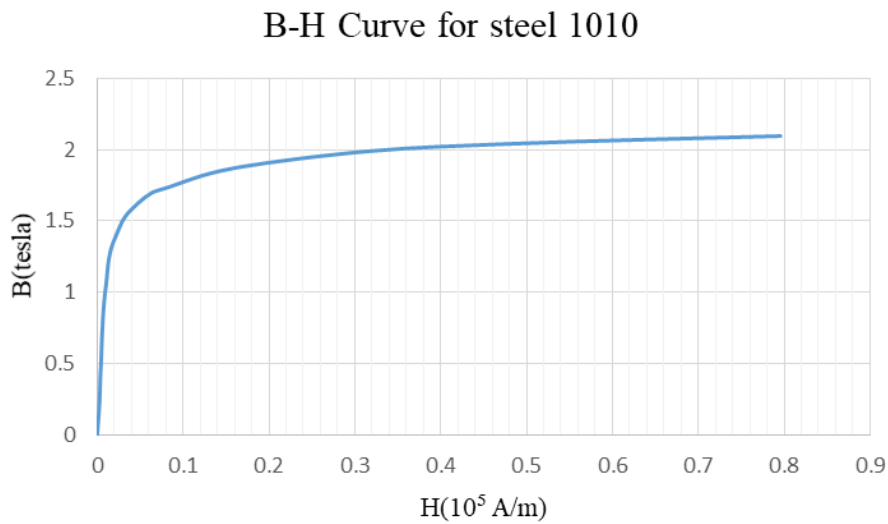**Fig. 6. The magnetic flux distribution inside the CVCA.**

Fig. 7. Nonlinear magnetization curve for steel 1010.

material of the various components of the CVCA and how they are assembled.

The magnetic flux density in various areas of the CVCA is depicted in Fig. 6. As can be seen, the magnetic flux density in most regions of the iron core is uniform, and the iron core's magnetic capacity is perfectly used.

Fig. 7 shows that the magnetization curve for steel 1010 has a linear behavior as long as the flux density is less than 1.5T, and enters the saturation zone for higher values. In Fig.6, it can be seen that no part of the iron core enters the saturation zone, and the electromagnetic saturation does not occur in this design.
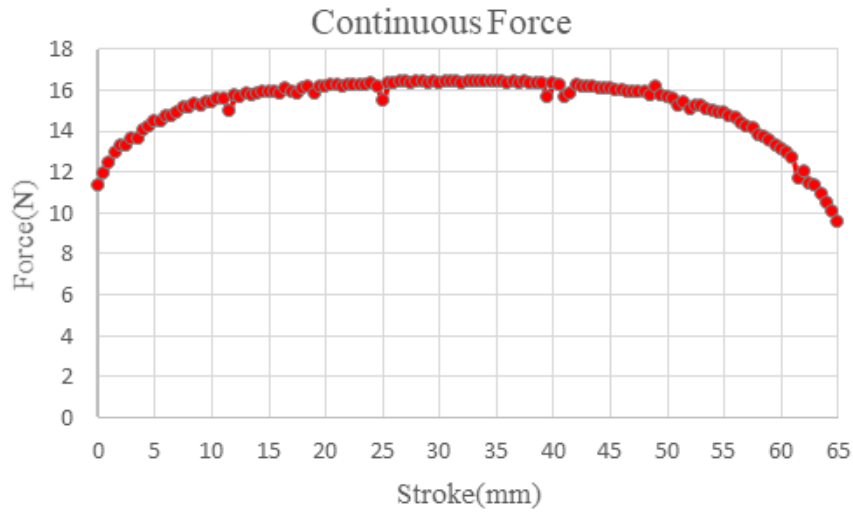
Fig. 8. The actuator's electromagnetic force versus rotor position when the coil's current density is 6 .
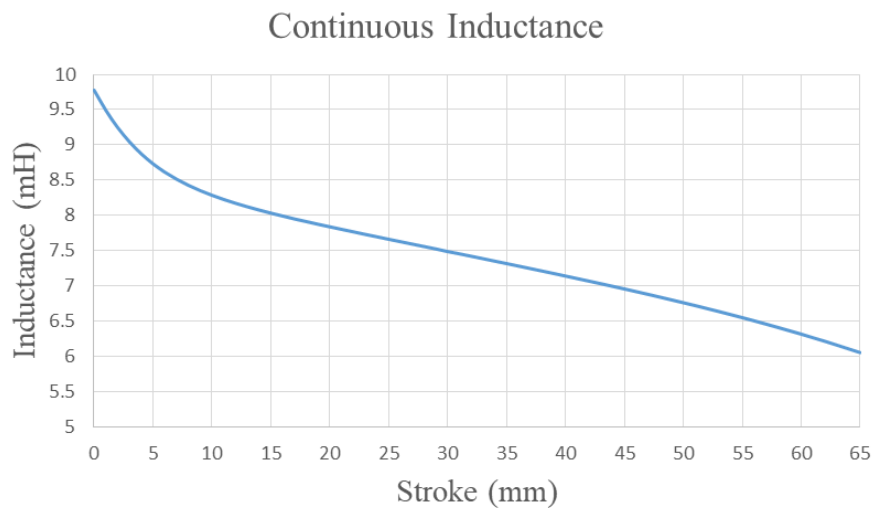

Fig. 9. The coil inductance versus rotor position.

Fig. 8 shows the CVCA force obtained using FEA at 0.5 mm intervals along the range of motion, assuming a coil current density of 6 A / mm^2 . It can be seen that the CVCA force is constant for most of the stroke length, and it is in the desired range. So, it can be said that the CVCA designed based on the optimization is able to generate the force considered in the design phase along the assumed stroke. Also, Fig. 9 depicts the coil's inductance changes over the CVCA stroke, which was also computed using FEA at 0.5 mm intervals over the actuator motion range and assuming a number of turns of 710.

3- Electromechanical design
3- 1- Mechanical design
Fig. 10 shows the Exploded view of the actuator. The magnet column consists of three pieces of off-the-shelf permanent magnets (NdFeB 42) glued together and connected to iron yokes at the bottom and top. The magnet wire (AWG#23) was coiled onto the machined aluminum (AL1080) rotor.

The mounting stage is installed on a sliding wagon and provides a platform for additional application-specific equipment to be attached.
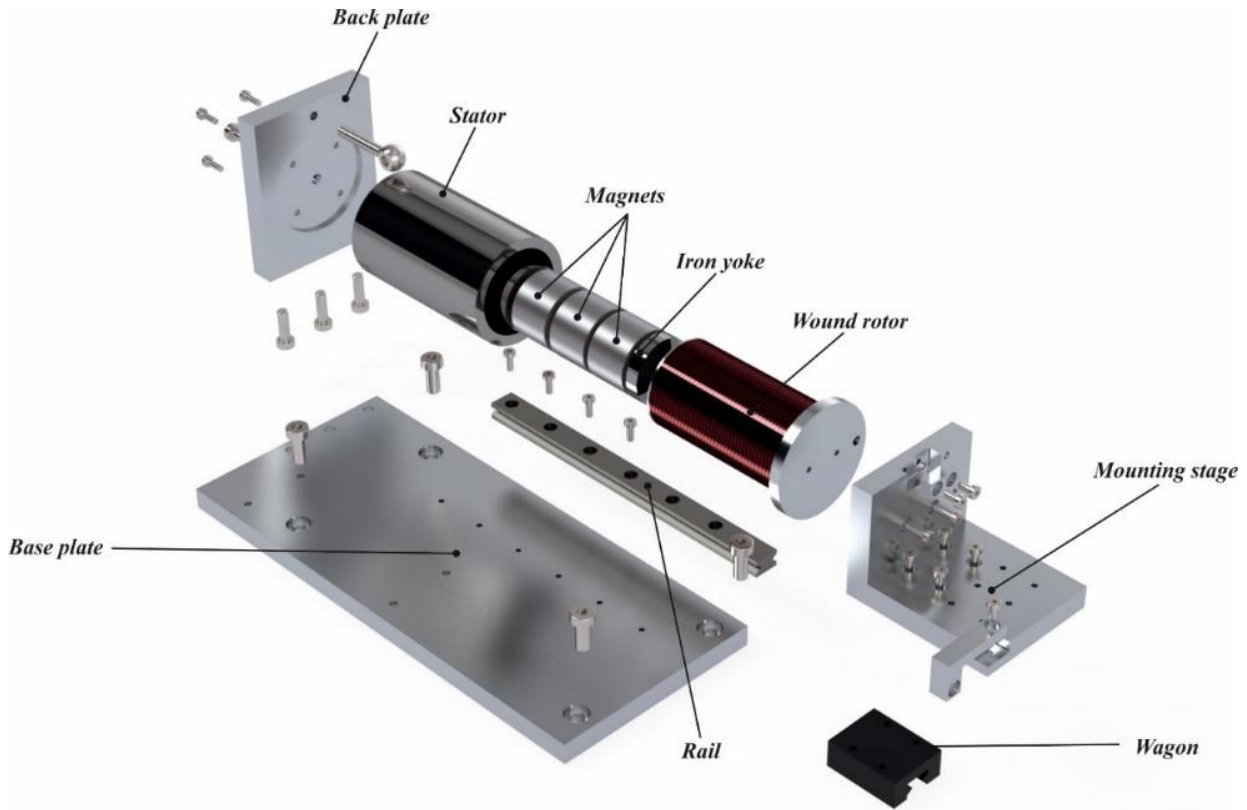
Fig. 10. The actuator's exploded view.

3- 2- Electrical design

The coil current should be regulated to control the electromagnetic force of the actuator. To attain this, two op-amps (TL072) and one power op-amp (OPA548T) were used to design an analog servo amplifier that outputs current proportional to the voltage command input. A 1-Ω sensing resistor (10 Watts) is used to feed back the current value to the circuit.

Fig. 12 shows the servo amplifier's frequency response for minimum and maximum coil inductance values. It could be recognized that the servo amplifier bandwidth stays above 10 kHz with a DC gain of 1.7, in spite of position-dependent variations of coil inductance.

3- 3- Instrumentation design

A linear potentiometer (sensor model) with infinite resolution and a maximum stroke of 100mm was employed to determine the rotor's position. The potentiometer's output voltage, which is proportional to the rotor position, is sampled by the microcontroller's 12-bit analog-to-digital converter. The microcontroller (STM32F407VGT6) is a 32-bit ARM Cortex M-4 with 1 MByte of flash memory and 192 KByte RAM which is utilized to implement the digital control algorithms. The computed control signal is transmitted to the servo amplifier through the microcontroller's 12-bit digital-to-analog converter. Fig. 13 depicts the main components of the system.

4- Characterization

4- 1- Force Constant

To determine the force constant, the rotor is set to prespecified positions and the coil current is set at I= 1 Amp. After that, a load cell is used to measure the electromagnetic force, as illustrated in Fig. 14.

The measured force and FEA results along the actuator stroke are shown in Fig. 15. The simulated force is slightly greater than the measured value which is due to friction and other assembly imperfections not accounted for in simulation.

The generated force was measured at different current levels for each position to determine the force constant. Fig.16 exhibits the force constant as a function of rotor position.

4- 2- Open-loop dynamics

The open-loop system dynamics are determined by injecting a chirp signal as a command to serve the amplifier and logging the corresponding rotor position.

The system's open-loop transfer function can be considered to be a second-order transfer function by ignoring the analog current controller's extremely fast dynamics:

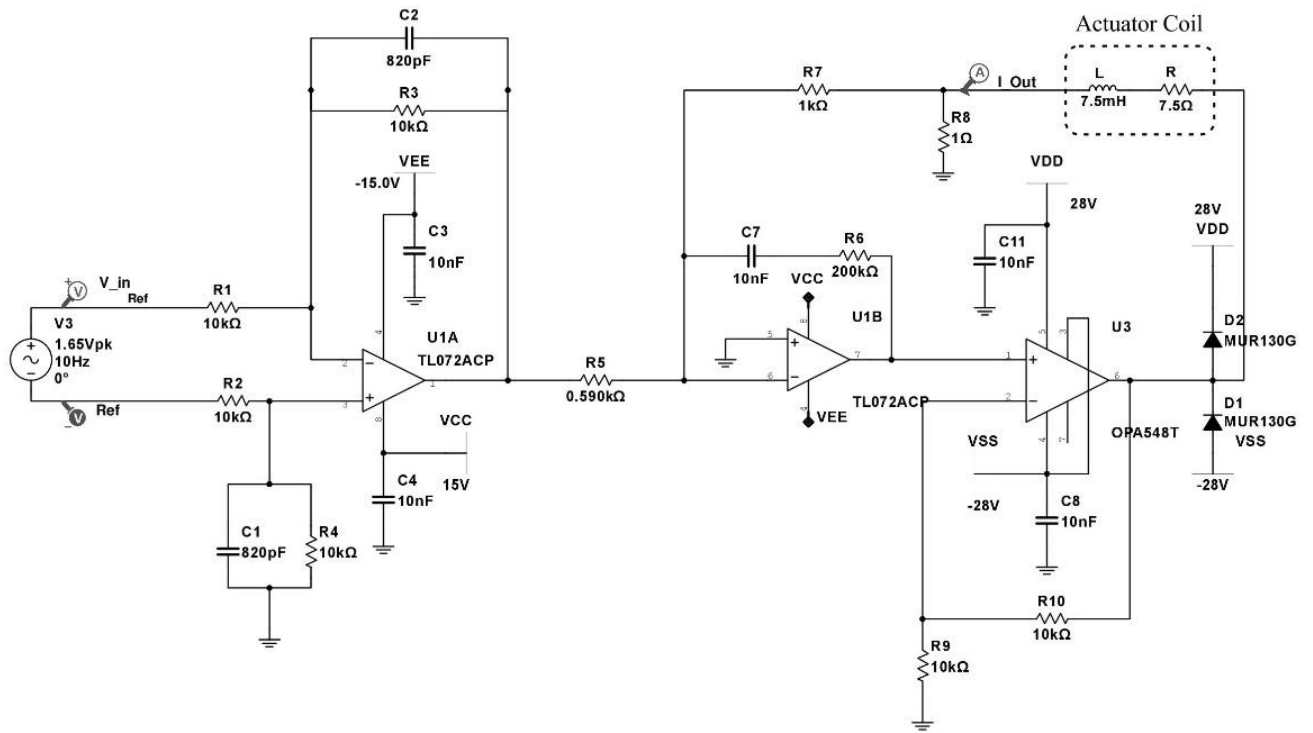$$G(s) = \frac{K}{s^2 + \frac{c}{m}s + \frac{k_s}{m}} \tag{17}$$
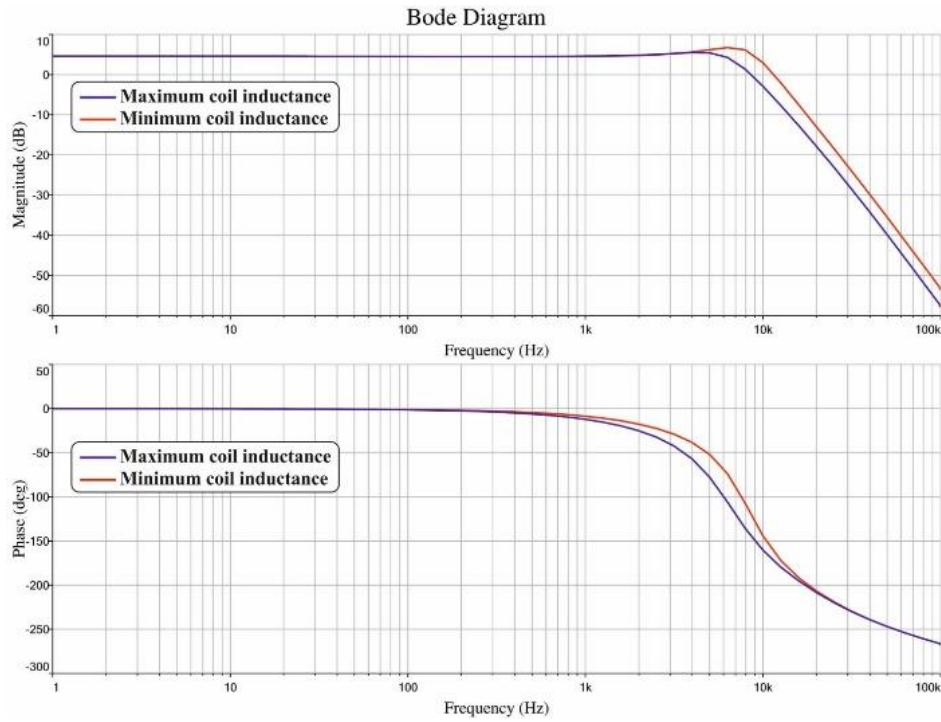
Fig. 11. Structure of the servo amplifier circuit.

Fig. 12. The servo amplifier's Bode diagram.
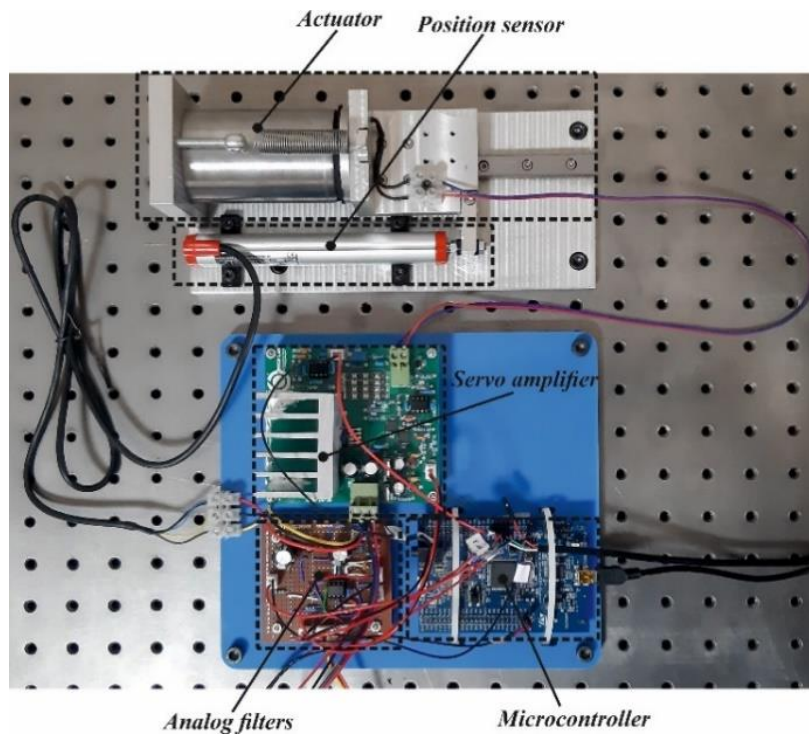
314
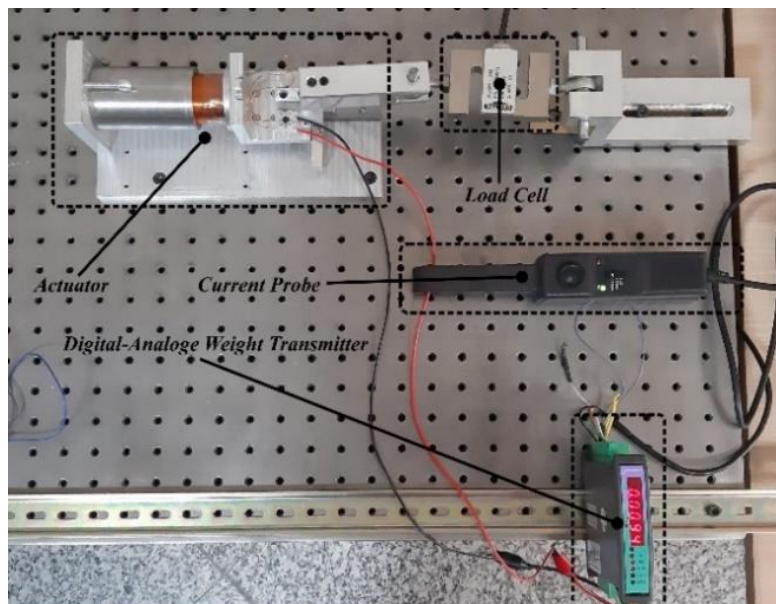
Fig. 13. Main parts of the system.

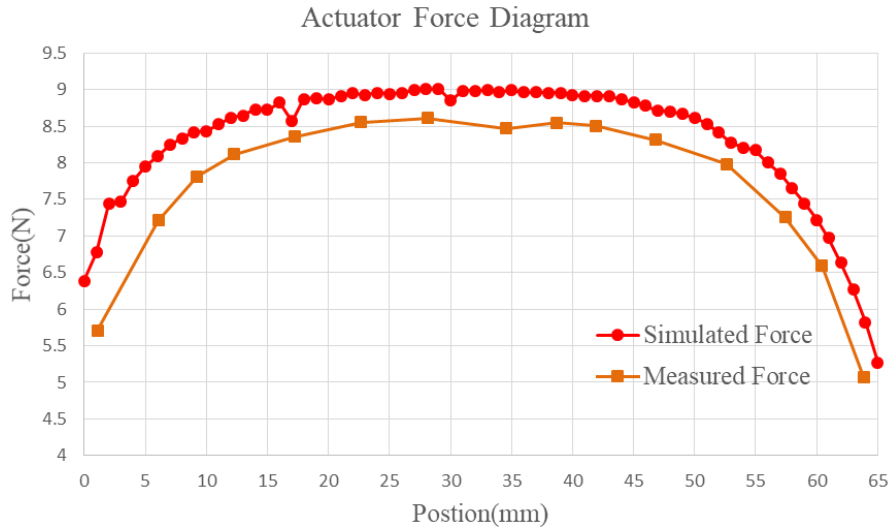**Fig. 14. The actuator force constant measurement setup.**

Fig. 15. Graphical comparison of the actuator's simulated and measured force.
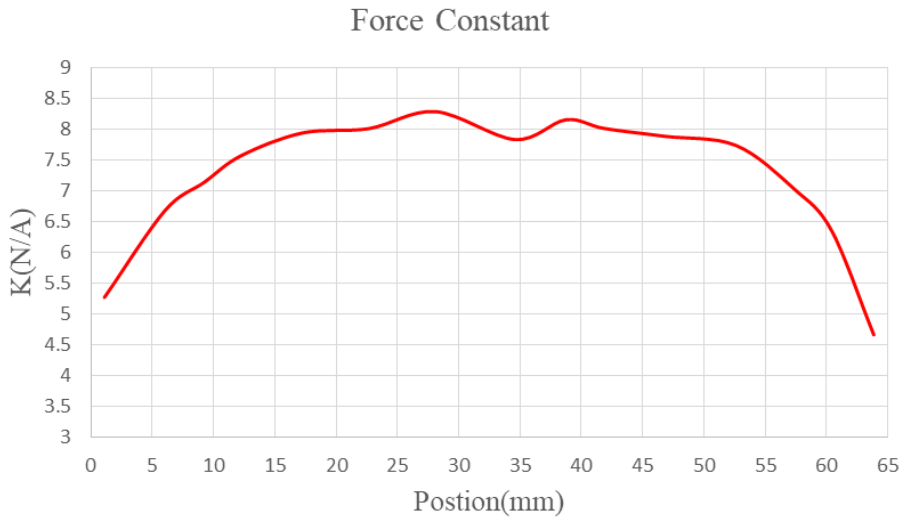

Fig. 16. Actuator force constant versus rotor position.

Where k_s, c and m represent the actuator spring constant, mechanical system damping, and mass of the moving part respectively, and K is the open-loop gain. The system input and output data in Fig. 17 are used to identify the system parameters. Resulting in the following transfer function:

$$G(s) = \frac{18726.56}{s^2 + 18.3664s + 103.1781}$$

Fig. 18 depicts the difference between the system's output and the output of the estimated transfer function. The output of the transfer function and the output of the actuator are almost identical, confirming that the estimated transfer function is valid. Eventually, the mechanical system damping and the actuator spring constant can be determined from the estimated transfer function by measuring the mass of the actuator moving part, according to (17).

5- Modeling

As a multi-domain system, the actuator's dynamics are determined by the interaction of several subsystems, as shown in Fig. 19.
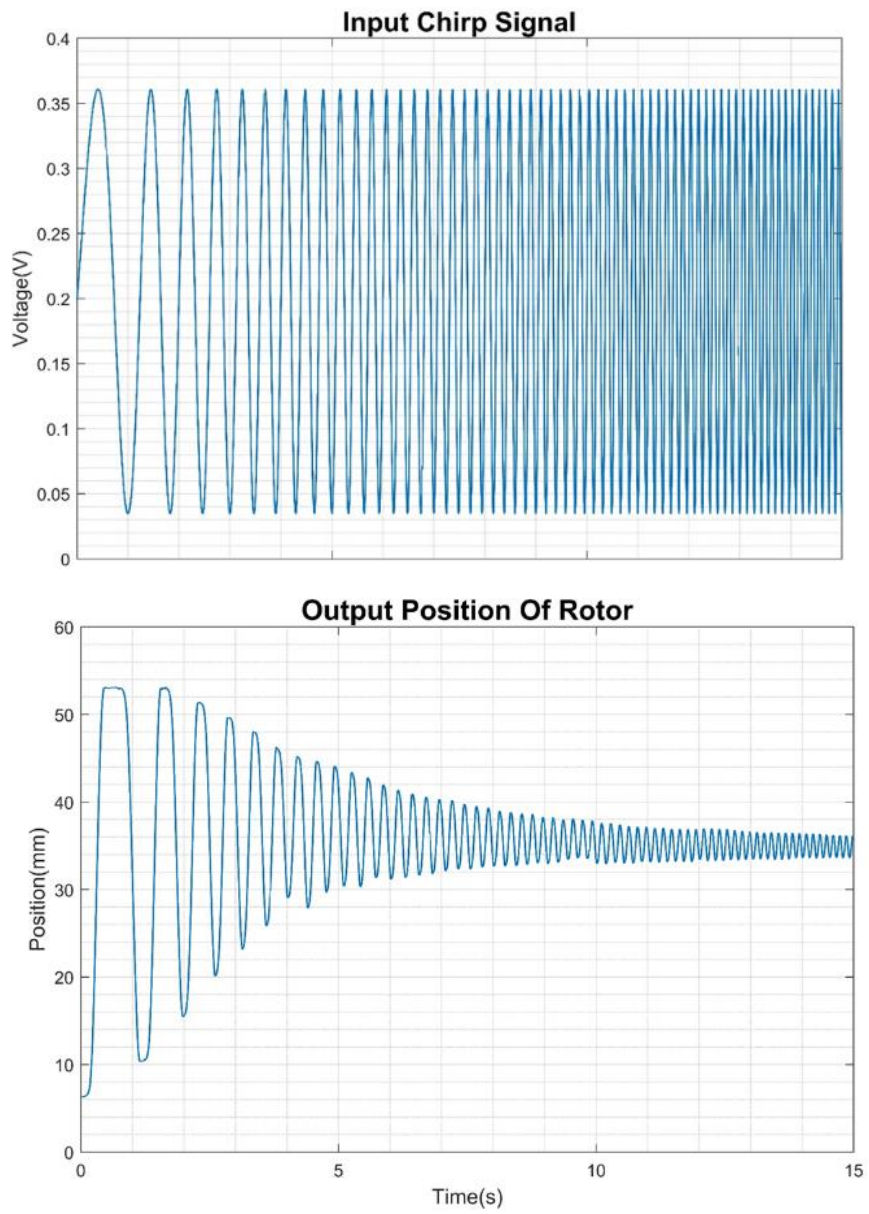
316

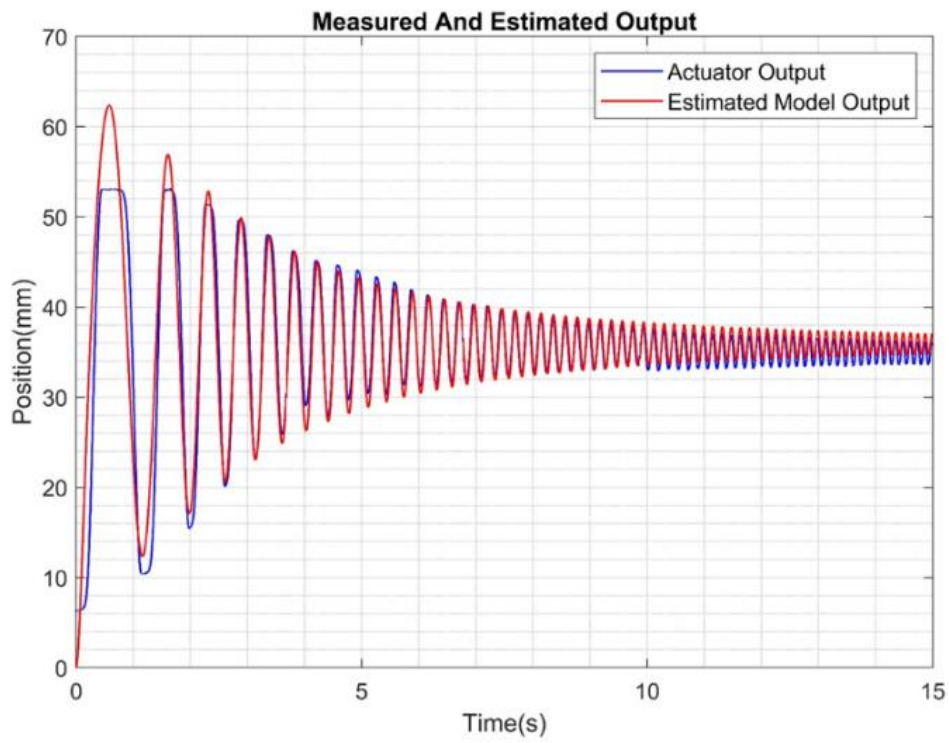**Fig. 17. Input and output data to identify the open loop system.**

Fig. 18. Comparison between estimated transfer function output and actuator output.
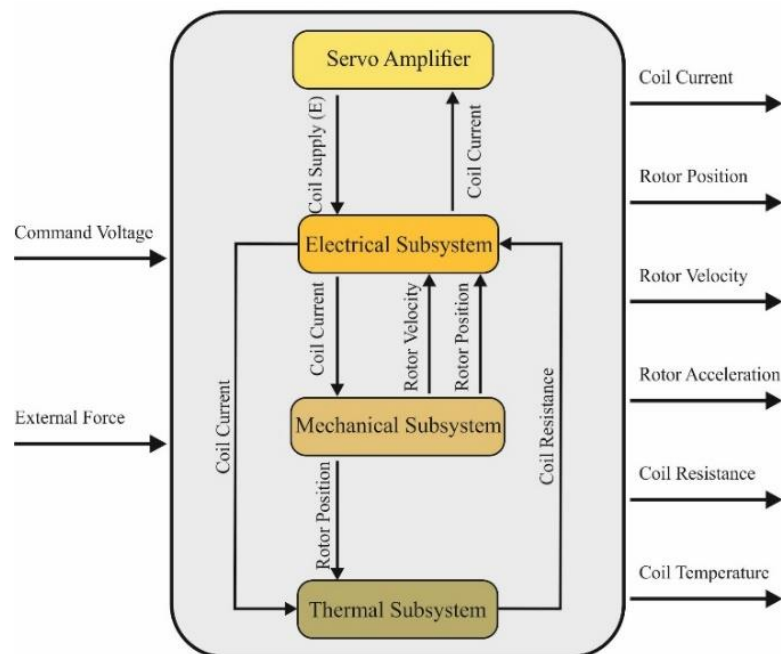

Fig. 19. The multi-domain voice coil actuator model.

Table 4. The most important parameters and their values.

Par	Definition	Unit	Value
m	Mass of the moving part	gram	523.8
c	Mechanical system damping	N.s / m	9.622
k_s	Spring constant	N.s / m	62.938
k_B	Back electromotive force constant	V.s / m	3
x_{min}	Lower band of rotor position	mm	0
x_{max}	Upper band of rotor position	mm	65
C_T	Coil thermal capacitance	J/K	83.098
R_0	Resistance at reference temperature	Ω	7.5
α_R	Temperature constant of coil resistance	K^{-1}	0.004041
K(x)	Force constant as a function of the rotor position	N / A	Fig. 16
L(x)	Inductance as a function of the rotor position	mH	Fig. 9

Physical parameters determined earlier using FEA or through characterization are required to model each of these subsystems. Table 4 shows a summary of these parameters.

5- 1- Servo amplifier

To derive the dynamic equations, we can write KVL and KCL equations based on servo amplifier circuit (Fig. 11) while using the ideal op-amp laws. So, the following is the transfer function between input, command voltage, and output, coil current:

$$\frac{I(s)}{V(s)} = \left(\frac{Z_1}{R_1 R_5} \right) \left(\frac{Z_2 (R_7 + R_8) \left(1 + \frac{R_{10}}{R_9} \right)}{Z_2 R_8 \left(1 + \frac{R_{10}}{R_9} \right) + Z_c (R_7 + R_8) + R_7 R_8} \right) \quad (18)$$

Where:

$$GZ_1 = R_3 \| C_2 = \frac{R_3}{R_3 C_2 s + 1} \quad (19)$$

$$Z_2 = R_6 + C_3 = \frac{R_6 C_7 s + 1}{C_7 s} \quad (20)$$

$$Z_c = R + L(x)s \quad (21)$$

5- 2- Electrical model

The actuator's basic electrical equation is:

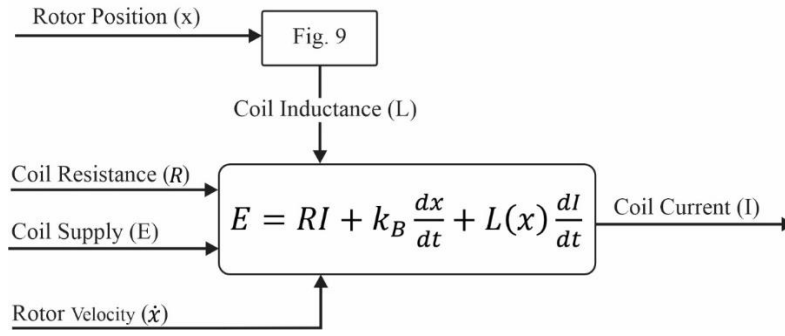$$E = RI + k_B \frac{dx}{dt} + L(x)\frac{dI}{dt} \quad (22)$$

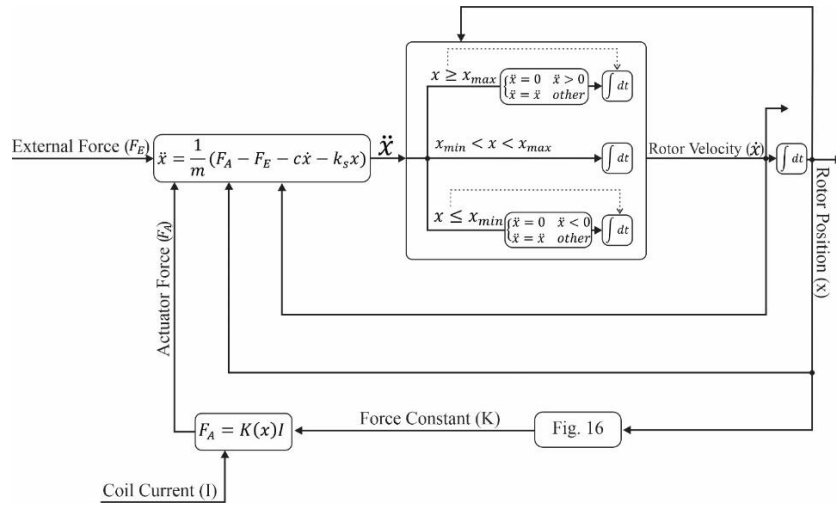**Fig. 20. The actuator's electrical subsystem.**

Fig. 21. The actuator's mechanical subsystem.

Where I represents the coil current, x is the rotor position E is the coil supply voltage, R is the coil resistance which is a function of the coil temperature, and k_B represents the back electromotive force (BEMF) constant. L also indicates the coil's inductance, which is dependent on the rotor position.

Fig. 20 depicts the electrical subsystem's architecture.

5- 3- Mechanical model

Using the Newton's second law, the equation of motion can be expressed as:

$$F_A - F_E = m\frac{d^2x}{dt^2} + c\frac{dx}{dt} + k_s x \qquad (23)$$

Where F_E indicates mechanical load and F_A represents the actuator force, which can be determined using the force constant:

$$F_A = K(x)I \qquad (24)$$

Fig. 21 depicts the architecture of the actuator mechanical subsystem.

In practice, the actuator can only move within its stroke's allowable range, and once it hits the upper or lower bound, regardless of coil current, it will stop. This phenomenon is taken into account in this model, and anytime the rotor position hits its upper (lower) bound, the rotor velocity is set to zero by resetting the acceleration integrator, and the acceleration itself is limited to non-positive (non-negative) values to avoid exceeding the actuator stroke's allowable range.

5- 4- Thermal model

Ohmic loss in the coil leads to temperature rise in the coil which in turn increases the coil resistance and corresponding loss. Hence, thermal management plays an important role in assuring reliable operation of the actuator and preventing premature failures. Also, the dynamics of the actuator are affected by altered coil resistance caused by temperature variations. The coil's thermal behavior is governed by the following equation:

$$P_D = \frac{\Delta T}{R_T} + C_T \frac{d\Delta T}{dt} \qquad (25)$$

Where C_T indicates the coil thermal capacitance and P_D is the coil's dissipated power, which is computed as follows according to Joule's first law.

$$P_D = R \times I^2 \tag{26}$$

In equation (25) ΔT also represents temperature variation, which is written as follows.

$$T = T_C - T_0 \tag{27}$$

Where T_0 is the initial coil temperature and T_C is the coil temperature. However, R_T, which indicates thermal resistance, is the most challenging parameter in (25). The method of heat transfer between the coil and the ambient must first be determined in order to calculate the value of R_T. Heat transfer by air via free convection is assumed to be the only heat transfer path for the coil in this case, and other heat transfer paths were ignored because of their remarkably high thermal resistance. So, to compute R_T, the film temperature is determined as:

$$T_f = \frac{T_c + T_\infty}{2} \tag{28}$$

Where T_∞ is the ambient temperature. Then thermal conductivity (k), Prandtl number (Pr), thermal diffusivity (α), and kinematic viscosity (ν) must be determined by utilizing the thermophysical properties of the air at the atmospheric pressure table according to the film temperature. Also, the volumetric thermal expansion coefficient (β) can be determined according to the following equation.

$$\beta = \frac{1}{T_f} \tag{29}$$

Then the Rayleigh number should be computed using the following equation.

$$Ra_D = \frac{g\beta(T_c - T_\infty)D^3}{\alpha\nu} \tag{30}$$

Where D indicates the coil diameter and g is the gravitational acceleration. The average Nusselt number is also calculated based on the following equation.

$$\overline{Nu_D} = \left\{ 0.6 + \frac{0.387 Ra_D^{1/6}}{\left[1 + (0.559/Pr)^{9/16}\right]^{8/27}} \right\}^2 \tag{31}$$

Equation (31) is represented to determine the average Nusselt number for an isothermal horizontal cylinder[24]. The average of the convection heat transfer coefficient is computed using the following equation after determining the average Nusselt number.

$$\bar{h} = \frac{k}{D}\overline{Nu_D} \tag{32}$$

Eventually, the thermal resistance can be computed as follows.

$$R_T = \frac{1}{\bar{h}\left(\frac{1}{4}\pi D^2 x\right)} \tag{33}$$

In Equation (33), because it is assumed that only the surface of the coil outside the stator cylinder transfers heat to the ambient and the part of the rotor within the stator cylinder is thermally insulated because of the thin layer of air that covers it, the heat transfer surface is determined by the rotor position (x).

After calculating thermal resistance, the coil temperature variation is computed by solving the (25), and the coil temperature can be determined from the initial coil temperature according to (27). In addition, the coil resistance can be computed as follows using the coil temperature variation.

$$R = R_0\left[1 + \alpha_R\Delta T\right] \tag{34}$$

Where α_R is the temperature constant of coil resistance and R_0 is the coil resistance at the initial coil temperature.

The architecture of the actuator thermal subsystem is shown in Fig. 22. This model calculates the thermal resistance of the coil employing (28), (29), (30), (31), (32), and (33) after receiving the rotor position from the mechanical model. It then solves equation (25) and computes the temperature variation of the coil by receiving the coil current from the electrical model, and then calculates the coil resistance by using (34) and sending it to the electrical model.

5- 5- Model validation

After defining each of the servo amplifier, electrical, mechanical, and thermal sub-models, a thorough model of the actuator can be created by putting them all together. In this part, we aim to validate the thorough model created for the actuator with the help of an experimental test. Intending to have better control over the actuator, we develop a digital lead controller for the actuator based on the open-loop transfer function identified in the previous section and test the model's performance with this controller in closed-loop mode. This digital lead controller's transfer function is as follows.
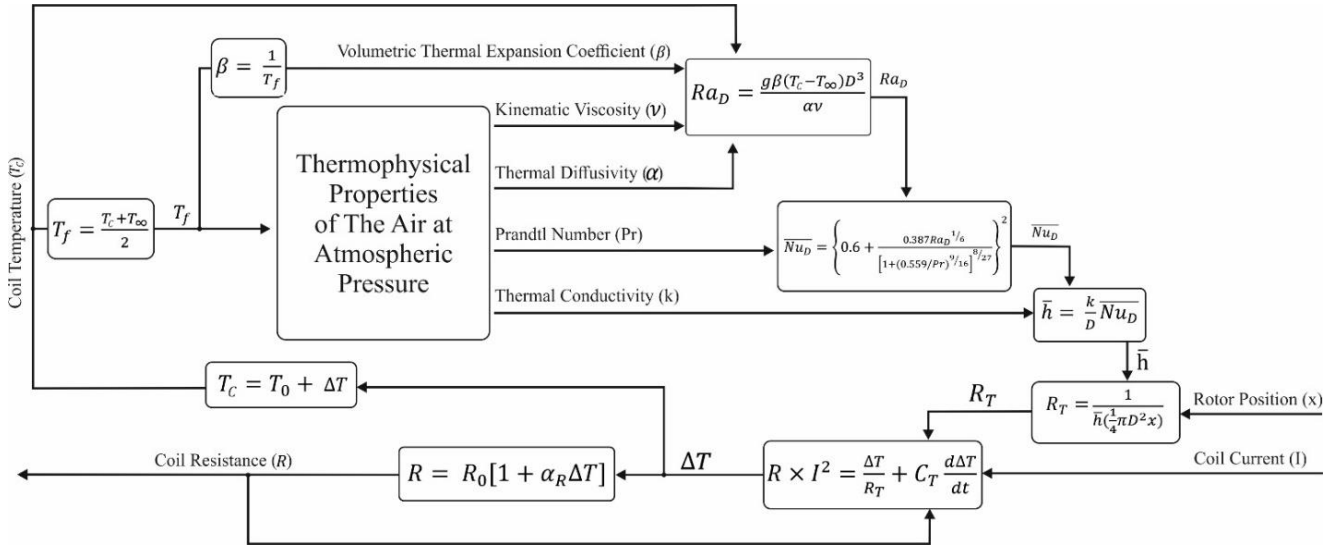
$$C(z) = 2.5372\frac{z - 0.9882}{z - 0.4212}$$

321

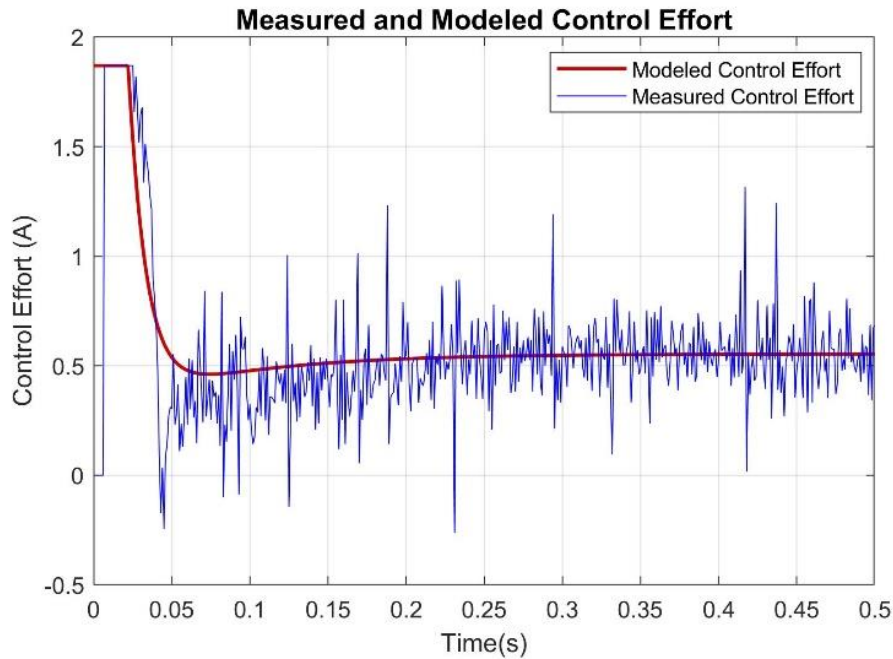**Fig. 22. The actuator's thermal subsystem.**

Fig. 23. Modeled and experimental control effort.

We determine a 50 mm step as a reference input to the closed-loop system, assuming the initial coil temperature is equal to the ambient temperature ($T_\infty = T_0 = 25°C$) and the external force is zero ($F_E = 0$). Based on the reference input and position feedback received from the actuator model, the digital lead controller determines the control effort and sends it to the actuator model as the command voltage. Besides, because the practical command voltage must be in the range of ±1.1 v, constraint also applies to modeling.

After implementing the digital lead controller by the

microcontroller, the 50 mm step is determined as a reference input to the experimental system, and the control effort and rotor position data are sampled. Following that, the data from the experiment is compared to the data from the modeling.

The modeled and measured control efforts for the actuator are shown in Fig. 23. The control effort calculated from the model is very similar to the measured control effort, as it is seen in this figure, and the slight differences are due to the impacts of position sensor high-frequency noise on the experimental control effort.
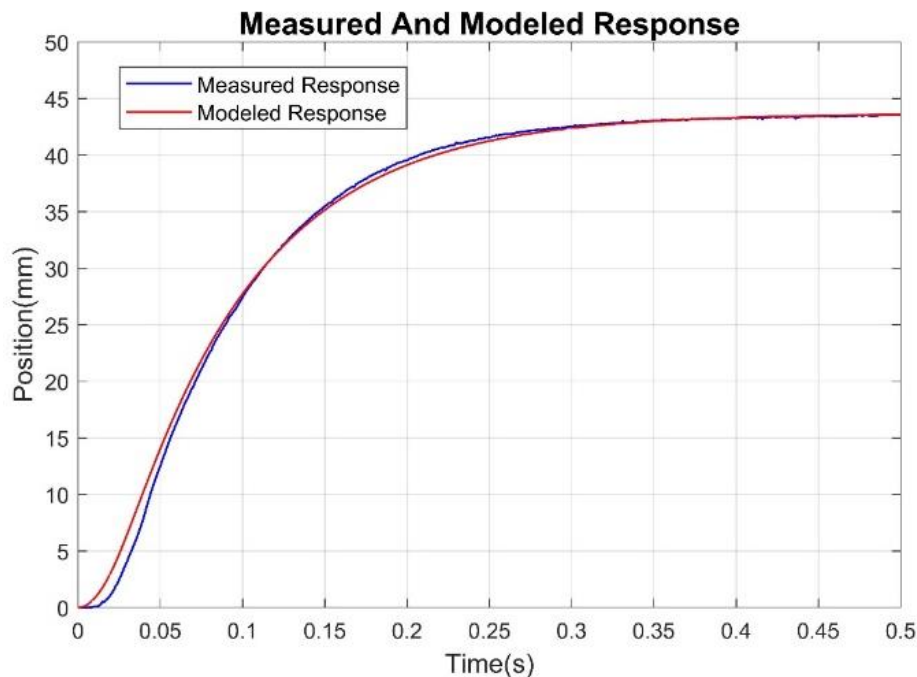
Fig. 24. Modeled and experimental rotor position.

Fig. 24 also depicts the rotor position calculated through modeling and the rotor position sampled by the position sensor. It can be observed that the findings are nearly identical.

As a result of Fig. 23 and Fig. 24, it can be concluded that the thorough model created for the actuator is capable of precisely modeling the actuator's behavior in experimental conditions.

6- Conclusion

Despite the advantages of CVCAs over other linear actuators and their diverse applications, there is a lack of optimal design methodology for these types of actuators. Also existence of an accurate model that can simulate their nonlinear dynamics, provides an invaluable platform for control system development while presenting an in-depth view of how all various subsystems interact.

In this paper, using the Maxwell equations governing CVCAs, the design problem was expressed in the form of a multi-objective optimization problem, and after solving this problem using NSGA-II, the optimal design was obtained from the Pareto optimal front and it is validated using electromagnetic finite-element analysis.

In the next step, according to the optimal magnetic design the electromechanical components of the actuator were designed followed by fabrication and assembly processes. The actuator characterization was then pursued which validated the optimal design and performance of the actuator.

Eventually, physics-based models of the various CVCA subsystems were developed, and a comprehensive model for the CVCA was created by integrating these models.

It was verified through experimental tests that this model can accurately mimic the actuator behavior making it an indispensable tool in designing advanced control systems.

References

[1] S. Saeedi, A. Sadighi, Digital Tracking Control of a Cylindrical Voice-Coil Actuator, in: 2022 10th RSI International Conference on Robotics and Mechatronics (ICRoM), 2022, pp. 291-295.

[2] T.Z.a.X.G. Y. Qiao, Overview of Position Servo Control Technology and Development of Voice Coil Motor, in: CES Transactions on Electrical Machines and Systems, pp. 269-278.

[3] W.J. L. Yong, H. Jianhui, W. Qian and L. Chengjun, Analysis of Factors Influencing Peak Torques and Peak Losses of Rotary Voice Coil Actuators Used in Aerospace, in: IEEE Access, 2021, pp. 57120-57126.

[4] C.-L.H.a.C.-S. Liu, Design of a Voice Coil Motor Actuator With L-Shape Coils for Optical Zooming Smartphone Cameras, in: IEEE Access, 2020, pp. 20884-20891.

[5] M.R. M. S. Zade, M. G. Nejad, S. Maleki and A. Sadighi, Optimal Design and Control of a Planar Voice-Coil Actuator for Micropositioning Applications, in: 2022 10th RSI International Conference on Robotics and Mechatronics (ICRoM), 2022, pp. 439-444.

[6] S. Saeedi, A. Sadighi, M.S. Panahi, Robust Repetitive Control of a Cylindrical Voice-Coil Actuator, in: 2021 9th RSI International Conference on Robotics and Mechatronics (ICRoM), 2021, pp. 281-286.

[7] J. McBean, C. Breazeal, Voice coil actuators for human-robot interaction, in: 2004 IEEE/RSJ International

Conference on Intelligent Robots and Systems (IROS) (IEEE Cat. No.04CH37566), 2004, pp. 852-858.

[8] S. Wu, Z. Jiao, L. Yan, R. Zhang, J. Yu, C.Y. Chen, Development of a direct-drive servo valve with high-frequency voice coil motor and advanced digital controller, in: IEEE/ASME Transactions on Mechatronics, 2014, pp. 932-942.

[9] O. Doaré, G. Kergourlay, C. Sambuc, Design of a circular clamped plate excited by a voice coil and piezoelectric patches used as a loudspeaker, in: Journal of Vibration and Acoustics, Transactions of the ASME, 2013, pp. 1-13.

[10] K.S. Ananthanarayanan, Third-Order Theory And Bang-Bang Control Of Voice Coil Actuators, in: IEEE Transactions on Magnetics, 1982, pp. 888-892.

[11] Y.D. Chen, C.C. Fuh, P.C. Tung, Application of voice coil motors in active dynamic vibration absorbers, in: IEEE Transactions on Magnetics, 2005, pp. 1149-1154.

[12] A. Okyay, M.B. Khamesee, K. Erkorkmaz, Design and optimization of a voice coil actuator for precision motion applications, in: IEEE Transactions on Magnetics, 2015.

[13] S. Ito, D. Neyer, S. Pirker, J. Steininger, G. Schitter, Atomic force microscopy using voice coil actuators for vibration isolation, in: IEEE/ASME International Conference on Advanced Intelligent Mechatronics (AIM), 2015, pp. 470-475.

[14] H.C. Yu, T.Y. Lee, S.J. Wang, M.L. Lai, J.J. Ju, D.R. Huang, S.K. Lin, Design of a voice coil motor used in the focusing a system of a digital video camera, in: IEEE Transactions on Magnetics, 2005, pp. 3979-3981.

[15] H. Gao, F. Zhang, W. Zeng, T. Dong, Z. Wang, Design and Optimization of Injector Based on Voice Coil Motor, in: SAE Technical Papers, 2017.

[16] Y. Hirano, J. Naruse, R. Tsuchiyama, Dynamic characteristics of a voice coil motor for a high performance disk drive, in: in IEEE Transactions on Magnetics, 1989, pp. 3073-3075.

[17] B.P. Ruddy, A.W. Dixon, R. Michael, J. Williams, A.J. Taberner, Optimization of Portable Electronically Controlled Needle-Free Jet Injection Systems, in: IEEE/ASME TRANSACTIONS ON MECHATRONICS, 2017, pp. 2013-2021.

[18] A.M.T. Corp, Optimization Design of a Voice Coil Actuator Based on Improved SOM, in: IEEE International Conference on Applied Superconductivity and Electromagnetic Devices Sydney, 2011, pp. 224-227.

[19] L. Encica, J. Makarovic, E.A. Lomonova, A.J.A. Vandenput, Space Mapping Optimization of a Cylindrical Voice Coil Actuator, in: IEEE TRANSACTIONS ON INDUSTRY APPLICATIONS, 2006, pp. 1437-1444.

[20] D.B. Roemer, M.M. Bech, P. Johansen, H.C. Pedersen, Optimum Design of a Moving Coil Actuator for Fast-Switching Valves in Digital Hydraulic Pumps and Motors, in: IEEE/ASME TRANSACTIONS ON MECHATRONICS, 2015, pp. 1-10.

[21] J.-k. Choi, H.-i. Lee, S.-y. Yoo, M.D. Noh, Analysis and Modeling of a Voice-Coil Linear Vibration Motor Using the Method of Images, in: IEEE TRANSACTIONS ON MAGNETICS, 2012, pp. 4164-4167.

[22] W. McMahan, K.J. Kuchenbecker, Dynamic Modeling and Control of Voice-Coil Actuators for High-Fidelity Display of Haptic Vibrations, in: IEEE Haptics Symposium, 2014, pp. 115-122.

[23] F. Baronti, A. Lazzeri, F. Lenzi, R. Roncella, R. Saletti, S. Saponara, Voice Coil Actuators : from Model and Simulation to Automotive Application, in: 35th Annual Conference of IEEE Industrial Electronics, 2009, pp. 1805-1810.

[24] S.W. Churchill, H.H.S. Chu, Correlating equations for laminar and turbulent free convection from a horizontal cylinder, in: International Journal of Heat and Mass Transfer, 1975, pp. 1049-1053.